

Importance of many body effects in the kernel of hemoglobin for ligand binding

Cédric Weber,^{1,2} David D. O'Regan,^{2,3} Nicholas D. M. Hine,^{2,4}
Peter B. Littlewood,^{2,5} Gabriel Kotliar,⁶ and Mike C. Payne²

¹King's College London, Theory and Simulation of Condensed Matter (TSCM), The Strand, London WC2R 2LS

²Cavendish Laboratory, J. J. Thomson Av., Cambridge CB3 0HE, U.K.

³Theory and Simulation of Materials, École Polytechnique Fédérale de Lausanne, Station 12, 1015 Lausanne, Switzerland

⁴Department of Materials, Imperial College London, Exhibition Road, London SW7 2AZ, U.K.

⁵Physical Sciences and Engineering, Argonne National Laboratory, Argonne, Illinois 60439, U.S.A.

⁶Rutgers University, 136 Frelinghuysen Road, Piscataway, NJ, U.S.A.

We propose a mechanism for binding of diatomic ligands to heme based on a dynamical orbital selection process. This scenario may be described as *bonding determined by local valence fluctuations*. We support this model using linear-scaling first-principles calculations, in combination with dynamical mean-field theory, applied to heme, the kernel of the hemoglobin metalloprotein central to human respiration. We find that variations in Hund's exchange coupling induce a reduction of the iron $3d$ density, with a concomitant increase of valence fluctuations. We discuss the comparison between our computed optical absorption spectra and experimental data, our picture accounting for the observation of optical transitions in the infrared regime, and how the Hund's coupling reduces, by a factor of five, the strong imbalance in the binding energies of heme with CO and O₂ ligands.

Metalloporphyrin systems, such as heme, play a central role in biochemistry. The ability of such molecules to reversibly bind small ligands is of great interest, particularly in the case of heme which binds diatomic ligands such as oxygen and carbon monoxide. Heme acts as a transport molecule for oxygen in human respiration, while carbon monoxide inhibits this function. Despite intensive studies [1–3], the binding of the iron atom at centre of the heme molecule to O₂ and CO ligands remains poorly understood. In particular, one problem obtained with density functional theory [4] (DFT) approaches to ligand binding of heme is that the difference in the binding energy ($\Delta\Delta E$) of carboxy-heme and oxy-heme is very large, and the theory predicts an unrealistic binding affinity to CO, several orders of magnitude larger than to O₂ [5, 6].

Recent progress has been made to cure this problem using DFT+ U for molecular systems [7, 8], with which it was found that the inclusion of many body effects in the calculations reduced the imbalance between O₂ and CO affinities [9]. Inclusion of conformational modifications, such as the Fe-C-O binding angle [10], or the deviation of the Fe atom from the porphyrin plane, were also shown to affect CO and O₂ binding energies.

A general problem encountered by DFT is the strong dependence of the energetics and the spin state on small changes in the geometry. In particular, traditional DFT fails to describe the correct high-spin ground state of heme molecules. DFT+ U provides an improved description [7, 11], but is known to overestimate magnetic moments and gives often artificial and non physical spin-symmetry-broken states. Moreover, the rotationally-invariant DFT+ U methodology does not capture well the effect of the Hund's coupling J , which is known to be large in iron based systems. It was recently shown that the effect of strong correlations are not always driven by

the Coulomb repulsion U alone, but in some cases act in combination with the Hund's coupling J [12–14]. Understanding the effect of strong correlations in heme, and in particular how the symmetry of the highest occupied molecular orbital (HOMO) is affected by U and J , is important in the context of describing the CO binding, which was shown to be strongly dependent on the HOMO symmetry [15].

Recent progress has been made in this direction by dynamical mean field theory [16] (DMFT), combined with DFT (DFT+DMFT) which can refine the description of the charge and spin of correlated ions, and describes in a remarkable way the strong correlations, induced by both U and J . Also, DFT can only describe a static magnetic moment associated with a spin symmetry broken state, and requires the inclusion of the spin-orbit interaction to explain a change of spin states [17]. This is not necessary at the DMFT level, which describes both static and fluctuating magnetic moments within the same framework.

In this work, we extend the DFT+ U analysis by means of the combination of state-of-the-art linear scaling DFT [18] with DMFT, and apply this methodology to heme. The methodology builds upon our earlier works [19] and is described in detail in the supplementary material.

Although DFT+DMFT has been widely used to study solids, in this study we apply our real-space DFT+DMFT implementation to a moderately large molecule, extending the scope of applicability of DMFT to biology in an unprecedented manner. DMFT allows the quantum and thermal fluctuations, missing in zero-temperature DFT calculations, to be recovered. Moreover, it includes within the calculation both the Coulomb repulsion U and the Hund's coupling J . Which of U or J drives the many body effects in heme [14] remains an open question, paramount to understanding ligand bind-

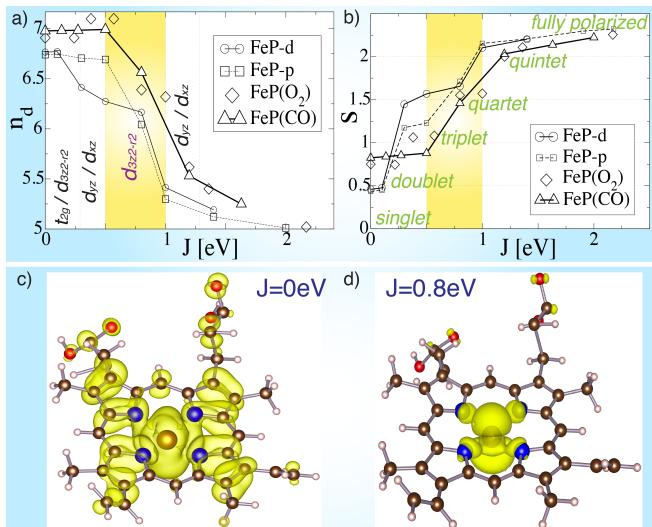


FIG. 1: **Orbital selection scenario:** Dependence of a) the iron 3d subspace occupancy n_d and b) the effective spin quantum number s on the Hund's coupling J , for both unligated and ligated heme models. The physically relevant region $0.5 \text{ eV} < J < 1 \text{ eV}$ is highlighted in yellow. Isosurfaces of the real-space representation of the electronic spectral density of the HOMO of FeP-d for c) $J = 0 \text{ eV}$ and d) $J = 0.8 \text{ eV}$. The large central sphere shows the location of the iron atom, and the four blue spheres indicate nitrogen atoms.

ing, that we address in this work. Methods are available to obtain U and J parameters appropriate to DMFT [20], but in this work we focus on the dependence of the results with the Hund's coupling J , and we verify that our calculations are not sensitive to the Coulomb repulsion U or to the temperature T [21]. The key question that we address in this work is: to what extent does the Hund's coupling, so far neglected in all studies applied to heme, affect the binding of heme to O_2 and CO ligands, and in particular does J reduce the strong affinity for CO binding? If not specified otherwise, we use a similar value $U = 4 \text{ eV}$ to those previously computed for $\text{DFT}+U$ [7], and ambient temperature $T = 294\text{K}$. The methodology is described in detail the supplementary material. Ionic geometries were obtained for four different configurations: unligated deoxyheme, FeP-d; the heme- CO complex carboxyheme, FeP(CO); the heme- O_2 complex oxyheme, FeP(O_2); and a theoretical planar version of deoxyheme, FeP-p.

We first discuss the dependence of the iron 3d subspace occupancy n_d on the Hund's coupling parameter J (Fig. 1.a). We emphasize that the expectation value of the occupancy n_d of the iron 3d sub-shell is not constrained to integer values in DFT and $\text{DFT}+\text{DMFT}$, since the iron occupation is a local observable, and hence does not commute with the Hamiltonian and is not conserved and there are valence fluctuations.

In the typical region of physically meaningful values of the Hund's coupling for iron 3d electrons, $J \approx 0.8 \text{ eV}$, [22] we find a very sharp dependence of the electronic density on J . In fact, $J \approx 0.8 \text{ eV}$ places heme directly in the tran-

sition region between low-spin states and the $n_d = 5$ e fully-polarized state obtained for large Hund's coupling. We note that our results are weakly dependent on the choice of the Coulomb repulsion U (see sup. material).

In Fig. 1.b, we show the effective quantum spin number, which is associated to the norm of the angular spin vector \mathbf{S} by the usual relation $|\mathbf{S}| = \sqrt{s(s+1)}$. The spin s shows characteristic plateaux as a function of the Hund's coupling at the semi-classically allowed values of the magnetization (corresponding to pure doublet, triplet, quartet, and quintet states). A fully-polarized state is recovered for sufficiently large Hund's coupling, as expected.

At $J = 0.8 \text{ eV}$, and almost irrespective of ligation and doming, we find that heme has a spin expectation value of $s \approx 1.5$ corresponding to a quartet state in a semi-classical picture. Our results indicate that the true many-body wave-function of FeP-d is thus an entangled superposition of triplet and quintet states. The proposition that heme might be in an entangled state was pointed out early [23] in the context of a Pariser-Parr-Pople model Hamiltonian, and is confirmed by our DMFT calculations. In particular, this accounts for the striking differences obtained experimentally for very similar porphyrin systems, e.g. it was found that unligated FeP is a triplet [24] in the tetraphenylporphine configuration, a triplet with different orbital symmetry in the octaethylporphine configuration [25], and a quintet in the octamethyltetrabenzporphine configuration [26]. The strong dependence of the spin state with respect to small modifications in the structure is consistent with an entangled spin state.

In our calculations, we find that both oxyheme and carboxyheme adopt a low spin state for $J < 0.25\text{eV}$ and larger multiplicities in the physical region of $J \approx 0.8\text{eV}$, while in both cases the spin state is very close in character to that of unligated deoxyheme. Significantly, we observe only subtle differences between FeP(O_2), FeP(CO) and FeP-d for $J = 0.8 \text{ eV}$, while the DFT and $\text{DFT}+U$ treatment yields ground-states for carboxyheme and oxyheme of pure closed-shell and open-shell singlet configurations, respectively [6, 7, 9].

Moreover, we find that the symmetry of the highest occupied molecular orbital (HOMO) of FeP-d, as estimated from the real-space spectral density of the prominent feature below the Fermi level, is highly dependent on the Hund's coupling J . In particular, for $J = 0 \text{ eV}$, the HOMO is an admixture of orbital characters (see vertical labels in Fig. 1.a). However, the Hund's coupling drives a rather complex orbital selection, such that for the region of greatest interest, $J \approx 0.8 \text{ eV}$, the HOMO predominantly exhibits $d_{3z^2-r^2}$ symmetry. The orbital selection process also induces a pinning of the Fermi density to the quantum impurity, such that it is delocalized for $J = 0 \text{ eV}$ (see Fig. 1.c), while for $J = 0.8 \text{ eV}$ (Fig. 1.d) it is instead localized to the iron 3d sub-shell.

In our view, this relates to the Fe-O-O angle obtained

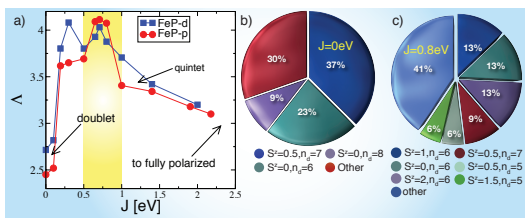


FIG. 2: **Valence fluctuations:** a) Von Neumann entropy Λ obtained by DFT+DMFT for FeP-p (circles) and FeP-d (squares). Histograms of the dominant electronic configurations for FeP-d for b) $J = 0$ eV and c) $J = 0.8$ eV. The pie wedge labelled *other* contains configurations with a weight smaller than 3%. The iron 3d spin S^z and iron 3d occupancy n_d of the dominant configurations is indicated.

in FeP(O₂) [27]. Indeed, the bent geometry of FeP(O₂) can be explained by a favorable interaction between the p*-orbital of the O₂ and the $d_{3z^2-r^2}$ -orbital on Fe [27]: the O₂ p*-orbital is closer in energy to $d_{3z^2-r^2}$ compared to the p*-orbitals in CO, and hence it gains more energy by bending, which increases the overlap. For FeP(CO) the situation is opposite, and there is no stabilization gained by bending [27]. On the contrary, the bending in FeP(CO) is induced by the strain of the protein and it reduces the binding energy. Naively, the orbital selection of the $d_{3z^2-r^2}$ orbital is hence expected to go in the direction of curing the strong O₂ and CO imbalance. Moreover, the charge localization at the Fermi level suggests that other artificial binding between the non-metallic atomic orbitals of heme and strong electronegative O₂ will not be obtained, and hence will protect heme from undesired charge transfer.

We now discuss the degree of quantum entanglement exhibited by FeP-d and FeP-p (see Fig. 2.a). We computed the von Neumann entropy $\Lambda = -\text{tr}(\hat{\rho}_d \log(\hat{\rho}_d))$, where $\hat{\rho}_d$ is the reduced finite-temperature density-matrix of the iron 3d impurity subspace, traced over the states of the AIM bath environment. The entropy quantifies to what extent the wave-function consists of an entangled superposition.

We observe that the entropy rises sharply at $J \approx 0.25$ eV, corresponding to the transition from the doublet spin state to the triplet/quintet entangled state. As expected, the entropy is small in the low-spin region ($J < 0.25$ eV) and also in the fully-polarized limit. At $J = 0$ eV (Fig. 2.b), we find that the dominant configuration consists of the doublets $(d_{3z^2-r^2})^2(d_{xy})^2(d_{xz})^2$, with a single electron in the $d_{x^2-y^2}$ orbital. The latter hybridizes strongly with the nitrogen 2p orbitals, but all other orbitals are mostly filled or empty, so this configuration is, essentially, a classical state with a finite magnetic moment.

At larger J values, however, such as $J = 0.8$ eV (Fig. 2.c), all orbitals are partially filled, and an increasing number of electronic configurations, with different valence and spin, contribute to the statistics, and thus the iron impurity wave-function is *fluctuating*. Although

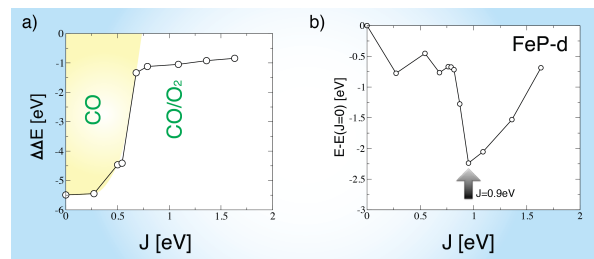


FIG. 3: **Energetics:** a) Difference in CO and O₂ binding energies $\Delta\Delta E$. The binding to CO is always favored, however the imbalance is strongly reduced for $J > 0.5$ eV. b) Total energy of FeP as a function of J . The minimum of the total energy is obtained for $J = 0.9$ eV.

the valence fluctuation are captured to some extent at the DFT level ($\Lambda_{DFT} \approx 0.75$), we find that many body effects contribute significantly to the entropy.

Our results indicate that as FeP-d and FeP-p molecules approach a regime with large entanglement for $J \approx 0.5$, with a concomitant orbital selection close to the Fermi level. The orbital selection close to the Fermi level in turn induces a charge-localization effect. The latter effect of the Hund's coupling can be understood with a simple picture: a large Hund's coupling partially empties the $d_{3z^2-r^2}$ orbital and brings the weight of this orbital closer to the Fermi level, thereby reducing the hybridization between the iron 3d states and the nitrogen 2p states close to the Fermi level. The subtle interplay between the charge-localization induced by the Hund's coupling (orbital selection close to the Fermi energy) and the delocalization induced by strong correlations (the tendency for electrons to escape the iron 3d orbitals in order to reduce the Coulomb energy) is captured by the DFT+DMFT methodology but is absent in Kohn-Sham DFT. We emphasize that these ingredients are paramount to an estimation of the charge transfer and binding properties between the iron atom and the ligand in oxyheme and carboxyheme.

Let us next discuss the effect of the Hund's coupling with respect to the unrealistic imbalance between the binding energies of CO and O₂ obtained by DFT. The binding energy is defined as: $\Delta E = E(\text{FeP}(X)) - (E(\text{FeP}) + E(X))$, where $X=\text{CO}$ or $X=\text{O}_2$. The difference between the binding energies $\Delta E(\text{CO}) - \Delta E(\text{O}_2)$ is obtained by: $\Delta\Delta E = \Delta E_{\text{CO}} - \Delta E_{\text{O}_2}$. For $J = 0$ eV, we find that the binding to CO is dramatically favoured, when compared to the binding to O₂ (Fig. 3.a): the difference in binding energies is of the order of 5 eV. Although the binding to CO is favoured for all values of J , we find that it is dramatically improved for $J > 0.5$ eV, and is reduced down to 1 eV. This suggests that other effects might be important to reduce further the CO/O₂ imbalance, such as that the effect of the protein via the bending of the Fe-C-O angle [9].

It is also worth noting that we find that the total energy of the molecule is minimized for $J = 0.9$ eV

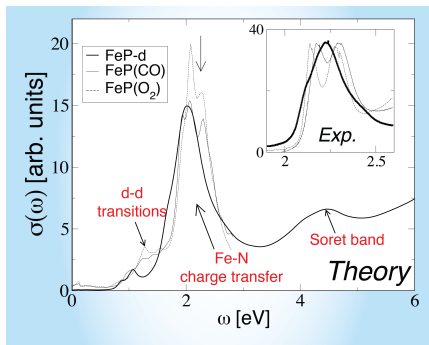


FIG. 4: **Optical measurements:** Optical conductivity of FeP-d (bold line) and FeP(CO) (solid) and FeP(O₂) (dashed line). The vertical arrow indicates the energy of the experimental peak associated to the Fe-N charge transfer. Inset: experimental measurements [28] for unligated heme (bold line), oxy- (dashed line) and carboxy- (solid) heme are shown for comparison. $J = 0.8\text{eV}$ was used for all calculations above.

(Fig. 3.b), suggesting further that the heme molecule is particularly well suited to host metallic d atoms, which tend to have a large screened J interaction when hybridising to light elements such as nitrogen or oxygen.

We now move to our calculations of the optical absorption spectra of heme (Fig. 4). Our theoretical absorption spectra, shown in Fig. 4, are in reasonable agreement with experimental data [28], in particular for the optical transitions at $\omega \approx 2\text{ eV}$. We attribute this spectral feature to charge-transfer excitations from iron to nitrogen-centered orbitals. The spectrum is dominated by the characteristic porphyrin Q-bands (those at $\approx 2\text{ eV}$), and Soret bands [29] (at $\approx 4\text{ eV}$). Our results offer insight into the infrared absorption band present at $\approx 1\text{ eV}$, in our calculation, and observed in experiments at 0.6 eV [30]. This infrared peak is described, in our calculations, as arising from transitions between the $d_{3z^2-r^2}$ spectral feature (HOMO) below the Fermi level and the LUMO (quasi-degenerate d_{xz} and d_{yz}) above the Fermi level.

Interestingly, we find that the infrared optical weight in unligated heme, associated with d - d transitions and present in FeP-d, is absent in the planar theoretical model FeP-p. Hence, the symmetry breaking associated with the doming effect of the iron-intercalated porphyrin macrocycle permits d - d optical transitions, and is responsible for the spectral weight in the infrared regime. We note that experimental spectra for FeP(CO) and FeP(O₂) exhibit a double peak structure at $\omega \approx 2\text{ eV}$, absent from our calculations done at $J = 0\text{ eV}$, but recovered for $J > 0.8\text{ eV}$. The best agreement with the experimental data is obtained for $J = 0.9\text{ eV}$. Finally, we extended our calculations to the time dependence of the magnetization of the iron atom after an initial quench in polarization (see sup. material). We propose that time-resolved spectroscopy may be used as a sensitive probe for the ligation state of heme.

In conclusion, we have carried out linear-scaling first-principles calculations, in combination with DMFT, on

both unligated and ligated heme. We have presented a newly-developed methodology applied to a molecule of important biological function, exemplifying how subtle quantum effects can be captured by our methodology. In particular, we have found that the Hund's coupling J drives an orbital selection process in unligated heme, which enhances the bonding in the out-of-plane direction. The von Neumann entropy quantifying valence fluctuations in the iron $3d$ subspace is large for the physical values of $J \approx 0.8\text{ eV}$. This scenario sheds some light on the strong CO and O₂ binding imbalance problem obtained by extracting the binding energies in simpler zero temperature and $J = 0\text{ eV}$ DFT calculations. The difference in binding energies is dramatically reduced for physical value of $J \approx 0.8$. The smaller remaining imbalance might be further explained by the strain energy contained in the protein structure [9] or by the contribution from the entropic term. Finally, the relevance of a finite Hund's coupling in heme is confirmed by the total energy extracted from the DFT+DMFT of unligated heme, which shows a minima for $J = 0.9\text{ eV}$.

We have proposed a new mechanism for ligand binding to heme based on an orbital selective process, on this basis, a scenario which we term *bonding determined by local valence fluctuations*. Finally, we have obtained a reasonable agreement between experimental and our theoretical optical absorption spectra, our description accounting for the observation of optical transitions in the infrared regime and the double peaked structure of the optical response at $\omega \approx 2\text{ eV}$.

At the time of writing, we became aware of related application of DMFT to an organometallic crystal [31]. We are grateful to R.H. McKenzie for comments and bringing Ref. [23] to our attention, and to D. Cole for many insightful discussions. C.W. was supported by the Swiss National Foundation for Science (SNFS). D.D.O'R. was supported by EPSRC. N.D.M.H was supported by EPSRC grant number EP/G055882/1. P.B.L is supported by the US Department of Energy under FWP 70069. Calculations were performed on the Cambridge High Performance Computing Service under EPSRC grant EP/F032773/1. Correspondence and requests for materials should be addressed to C.W.

-
- [1] A. M. P. Sena, V. Brázdrová, and D. R. Bowler, *Phys. Rev. B* **79**, 245404 (2009).
 - [2] D. D. O'Regan, N. D. M. Hine, M. C. Payne, and A. A. Mostofi, *Phys. Rev. B* **82**, 081102 (2010).
 - [3] P. M. Oppeneer, P. M. Panchmatia, B. Sanyal, O. Eriksson, and M. E. Ali, *Progress in Surface Science* **84**, 18 (2009).
 - [4] W. Kohn and L. J. Sham, *ibid.* **140**, A1133 (1965).
 - [5] D. Benito-Garagorri, I. Lagoja, L. F. Veirosb, and K. A. Kirchner, *Dalton Trans.* **40**, 4778 (2011).

- [6] C. Rovira, P. Ballone, and M. Parrinello, *Chem. Phys. Lett.* **271**, 247 (1997).
- [7] D. A. Scherlis, M. Cococcion, P. Sit, and N. Marzari, *J. Phys. Chem. B* **111**, 7384 (2007).
- [8] H. J. Kulik, M. Cococcioni, D. A. Scherlis, and N. Marzari, *Phys. Rev. Lett.* **97**, 103001 (2006).
- [9] D. J. Cole, D. D. O'Regan, and M. C. Payne, *J. Phys. Chem. Lett.* **3**, 1448 (2012).
- [10] C. Rovira and M. Parrinello, *Chem. A Eur. J.* **5**, 250 (1999).
- [11] P. M. Panchmatia, M. E. Ali, B. Sanyal, and P. M. Oppeneer, *J. Phys. Chem. A* **114**, 13381 (2010).
- [12] Z. P. Yin, K. Haule, and G. Kotliar, *Nat Phys* **7**, 294 (2011).
- [13] L. de' Medici, *Phys. Rev. B* **83**, 205112 (2011).
- [14] L. de' Medici, J. Mravlje, and A. Georges, *Phys. Rev. Lett.* **107**, 256401 (2011).
- [15] G. Kresse, A. Gil, and P. Sautet, *Phys. Rev. B* **68**, 073401 (2003).
- [16] A. Georges, G. Kotliar, W. Krauth, and M. J. Rozenberg, *Rev. Mod. Phys.* **68**, 13 (1996).
- [17] H. Nakashima, J.-Y. Hasegawa, and H. Nakatsuji, *J. Comput. Chem.* **27**, 426 (2006).
- [18] C.-K. Skylaris, A. A. Mostofi, P. D. Haynes, O. Diéguez, and M. C. Payne, *Phys. Rev. B* **66**, 035119 (2002).
- [19] C. Weber, D. D. O'Regan, N. D. M. Hine, M. C. Payne, G. Kotliar, and P. B. Littlewood, *Phys. Rev. Lett.* **108**, 256402 (2012).
- [20] L. Vaugier, H. Jiang, and S. Biermann, [arXiv/1206.3533](https://arxiv.org/abs/1206.3533) (2012).
- [21] See Supplemental Material at <http://link.aps.org/supplemental/10.1103/PhysRevLett.000.000000> for the methodology and additional data.
- [22] A. Kutepov, K. Haule, S. Y. Savrasov, and G. Kotliar, *Phys. Rev. B* **82**, 045105 (2010).
- [23] D. A. Case, B. H. Huynh, and M. Karplus, *Journal of the American Chemical Society* **101**, 4433 (1979), <http://pubs.acs.org/doi/pdf/10.1021/ja00510a001>.
- [24] G. Lang, K. Spartalian, C. A. Reed, and J. P. Collman, *J. Chem. Phys.* **69**, 5424 (1978).
- [25] J. P. Collman, J. L. Hoard, N. Kim, G. Lang, and C. A. Reed, *J. Am. Chem. Soc.* **97**, 2676 (1975).
- [26] J. R. Sams and T. B. Tsin, *Chem. Phys. Lett.* **25**, 599 (1974).
- [27] D. T. R. Hoffmann, M.M.-L. Chen, *Inorg. Chem.* **16**, 503 (1977).
- [28] J. M. Steinke and A. P. Shepherd, *Clin. Chem.* **38**, 1360 (1992).
- [29] R. Schweitzer-Stenner, J. P. Gorden, and A. Hagarman, *J. Chem. Phys.* **127**, 135103 (2007).
- [30] M. D. Kamen, T. Kakuno, R. G. Bartsch, and S. Hannon, *Proc. Nat. Acad. Sci.* **70**, 1851 (1973).
- [31] J. Ferber, K. Foyevtsova, H. O. Jeschke, and R. Valenti, [arXiv/1209.4466](https://arxiv.org/abs/1209.4466) (2012).

Importance of many body effects in the kernel of hemoglobin for ligand binding

Cédric Weber,^{1,2} David D. O'Regan,^{2,3} Nicholas D. M. Hine,^{2,4}
Peter B. Littlewood,^{2,5} Gabriel Kotliar,⁶ and Mike C. Payne²

¹King's College London, Theory and Simulation of Condensed Matter (TSCM), The Strand, London WC2R 2LS

²Cavendish Laboratory, J. J. Thomson Av., Cambridge CB3 0HE, U.K.

³Theory and Simulation of Materials, École Polytechnique Fédérale de Lausanne, Station 12, 1015 Lausanne, Switzerland

⁴Department of Materials, Imperial College London, Exhibition Road, London SW7 2AZ, U.K.

⁵Physical Sciences and Engineering, Argonne National Laboratory, Argonne, Illinois 60439, U.S.A.

⁶Rutgers University, 136 Frelinghuysen Road, Piscataway, NJ, U.S.A.

In this supplemental material, we study the dynamical magnetic response of heme, in various ligation and doming configurations, by means of out-of-equilibrium calculations performed by perturbing the DFT+DMFT ground state wave-function and propagating in the Keldysh time domain. Based on the rather strong ligand specificity observed in these simulations, we propose a potentially sensitive method for profiling of heme binding, using two-photon circularly-polarized spectroscopy. Here, we also describe the theoretical methods used in the work presented in our Letter in detail, and justify the range of parameters used in our study, i.e. we explore the dependence of our calculations on the choice of the Coulomb repulsion and the temperature. A simple toy model for calculating the entropy is proposed, and compared to the DMFT calculations, in order to illustrate the importance of many body effects. We furthermore justify the importance of the Hund's coupling based on phenomenological grounds, by carryout a comparison between the theoretical optics at various values of the Hund's coupling with experiments. Out-of-equilibrium calculations are also discussed.

In this work, we have carried out a detailed theoretical study of the electronic structure of the heme molecule by means of a combination [1, 2] of linear-scaling density-functional theory (DFT) with the dynamical mean-field theory approximation (DFT+DMFT) [3, 4], a model which includes local dynamical, finite-temperature and multi-determinantal effects, for given Hamiltonian parameters, at an effectively exact level. Although DFT+DMFT has been primarily applied to solids to date, here we apply our real-space DFT+DMFT implementation to a substantial molecular system, extending the scope of DFT+DMFT applicability to biology for the first time to our knowledge. We performed a study of the impact of varying the Hund's exchange coupling strength J . Although the value of J in iron based molecules and solids is expected to be $J \approx 0.8$ eV, [5, 6] we are interested in this work to study what are the physical ingredients introduced by J as it is increased from zero. In particular, it was suggested that the Hund's coupling might fix the strength of the correlations [7], or act to increase the total magnetic moments within the localized effective impurity subspaces treated using DMFT and, in doing so, break degeneracies between the localized orbitals.

The effects on the electronic structure due to the diatomic axial ligands O_2 and CO are considered, and testing is further carried out with respect to changes in the Hubbard U parameter and temperature. Our study furthermore includes two experimental signatures of ligand binding, namely the optical conductivity discussed in our Letter, and the transient magnetic response with which we discuss at the end of this supplemental material.

METHODOLOGY: DENSITY-FUNCTIONAL THEORY CALCULATIONS USING OPTIMIZED WANNIER FUNCTIONS

Kohn-Sham density-functional theory (DFT) [8, 9] was used in this study to provide a reasonable, conveniently-computed zero-temperature, single-determinantal starting point for the DFT+DMFT self-consistency procedure, within the localized subspace treated for many-body effects using DMFT, as well as a sufficiently detailed description of the delocalized electron "bath" comprising the remainder of the system. Relatively simple local and semi-local approximate functionals for DFT often provide an acceptably refined description of the ground-state electronic structure, and even the quasi-particle band-structure, associated with orbitals of large spread or no magnetic order. This observation forms the basis of the DFT+DMFT approximation, in which the dominant computational effort is instead focused on solving for the many-body wave-function constructed from the the remaining, localized, possibly spin-polarized orbitals adjacent to the Fermi-level.

The ONETEP linear-scaling DFT and DFT+ U code [10–12] was used to solve for the DFT ground-state subspace Green's function in this work. The ONETEP method is based on direct minimization of the total-energy with respect to the single-particle density-matrix, and is particularly advanced in terms of its accuracy equivalent to that of a plane-wave method, which is arrived at by means of an *in situ* variational optimization of the expansion coefficients of a minimal set of spatially-truncated Nonorthogonal Generalized Wannier Functions [13] (NGWFs) $\{\phi_\alpha\}$ (with non-trivial overlap $S_{\alpha\beta} = \langle \phi_\alpha | \phi_\beta \rangle$). The basis for this expansion is a set

of systematically improvable Fourier-Lagrange, or psinc functions [14], which is equivalent to a truncated set of plane-waves. We express the single-particle density-matrix in the separable form [15, 16] given by

$$\rho_0(\mathbf{r}, \mathbf{r}') = \sum_{\alpha\beta} \phi_\alpha(\mathbf{r}) K^{\alpha\beta} \phi_\beta(\mathbf{r}'), \quad (1)$$

where $K^{\alpha\beta} = \langle \phi^\alpha | \hat{\rho}_0 | \phi^\beta \rangle$ is known as the density-kernel, the tensor representation of the single-particle density operator $\hat{\rho}_0$ [58]. The contravariant NGWF duals $\{\phi^\alpha\}$ are defined as those which satisfy the biorthonormality relation, where the overlap matrix acts as metric tensor, defined by

$$\langle \phi^\alpha | \phi_\beta \rangle = \delta_{\beta}^{\alpha}, \quad \text{with} \quad |\phi^\alpha\rangle = (S^{-1})^{\alpha\beta} |\phi_\beta\rangle. \quad (2)$$

The use of a minimal, optimized Wannier function representation of the density-matrix allows for the DFT ground state to be solved with relative ease in large systems, particularly in molecules where their explicit truncation implies that the addition of vacuum does not increase the computational cost. Furthermore, it allows for the full Kohn-Sham Green's function to be computed via Hamiltonian inversion with a manageable computational overhead. Thus, we do not make any projection over bands or orbitals prior to generating the full Green's function, and only project after inversion when computing the matrix elements of the subspace Green's function.

METHODOLOGY: IONIC GEOMETRIES, PSEUDOPOTENTIALS AND VARIATIONAL PARAMETERS

We performed ground-state DFT calculations on heme *in vacuo* by iteratively minimizing the energy functional with respect to both the density kernel and the NGWFs, using the algorithm described in Ref. [17]. The total-energy was converged to within 1 meV per atom, with respect to the plane-wave energy cutoff (at a minimum of 1300 eV for all reciprocal lattice vectors in our calculations) and the NGWF cutoff radii (at 6.6 Å for all species), and no additional restrictions on the variational freedom, such as the density kernel truncation, were invoked. The simulation cell volume was increased until (at $4.8 \times 10^4 \text{ \AA}^3$) periodic-image interaction errors also fell within this total-energy tolerance.

The DFT calculations were performed, and pseudopotentials generated, using the PBE [18] generalized gradient exchange-correlation functional. In line with common practice in DFT+DMFT calculations, in which all magnetic order is assumed to be confined to the localized impurity subspaces, spin-degenerate DFT ground-state densities were used. Scalar relativistically corrected norm-conserving PBE [18] pseudopotentials, generated with the OPIUM package [19], were used in

place of the core electrons for all ions. The semi-core states of iron were included in the valence, so that the (3s,3p,3d,4s,4p) sub-shells were retained for explicit treatment, obviating the use of a non-linear core correction. For the lighter element, (2s,2p) were retained in the valence for C, N, and O, along with (1s) for H. Hence, we used 13 variationally-optimized NGWFs to describe the Fe electrons, 4 NGWFs for each C, N, and O atom, and 1 for each H atom, giving a total of 213 NGWFs (spin-degenerate orbital pairs) for the unligated heme system and 221 each for the two ligated systems.

Ionic geometries were obtained from the Protein Data Bank: unligated deoxyheme (dome-shape, FeP-d) was extracted from a human deoxyhaemoglobin structure obtained by x-ray crystallography (PDB key 2HHB [20]), and the missing hydrogens were reintroduced using the Jmol package [21]. The Carboxyheme (heme-CO complex, FeP(CO)) and the oxyheme (heme-O₂ complex, FeP(O₂)) structures were extracted using the same procedure (PDB key 1GCW [22] and 1HHO [23], respectively). A theoretical, planar deoxyheme (FeP-p) (PDB key HEM) is also considered in our calculations for comparison with the experimentally-observed dome-shaped structure in order to test how the conformal change between the planar and dome-shape affects the electronic structure. In the present work, we limit our calculations to a single heme molecule, omitting residues which neighbour it in the haemoglobin protein.

METHODOLOGY: DEFINITION OF THE LOW-ENERGY, CORRELATED MODEL

We extended our DFT calculations using the DFT+DMFT method [3, 4] in order to refine the description of strong correlation effects arising due to partial degeneracies between the localized orbitals making up the iron 3d sub-shell at the core of heme. DMFT allows for quantum and thermal fluctuations, absent from the zero-temperature, single-determinant Kohn-Sham DFT calculations, to be accurately described. The heme molecule was represented within DMFT by an Anderson impurity Hamiltonian (AIM) [24], in its Slater-Kanamori form, the ground-state of which was solved for by using a finite-temperature Lanczos solver [25]. Since only a single impurity site (3d orbital subspace) is present, the system becomes crystal momentum independent in the molecular limit, and since the Kohn-Sham Green's function is inverted in full before projection onto the impurity subspace, the Anderson impurity mapping is effectively exact, so that the DFT+DMFT algorithm is almost entirely converged in a single Green's function self-consistency step. We note that a Kondo model was used early in the literature to study heme, along similar lines than ours, by means of a model Hamiltonian [24]. In our study, the AIM model is determined and obtained by first-principle

calculations.

A spherically symmetric trial impurity subspace was defined by a spanning set of iron $3d$ orbitals, the orthonormal set $\{\varphi_m\}$ produced by solving the spherically-symmetric Schrödinger equation subject to the norm-conserving iron pseudopotential with an appropriate confining potential, the within a truncation sphere of radius 6.6 \AA . The same procedure was used to generate the initial guesses for the NGWFs during the initialization of the DFT calculation, so that the trial impurity subspace formed a proper subspace of the initial guess for the Kohn-Sham Hilbert space. Since the latter is optimized as the energy is minimized with respect to the NGWFs, so, at convergence of the DFT algorithm, the Hubbard projectors finally chosen to span the impurity subspace of DFT+DMFT were the so-called symmetry-adapted Nonorthogonal Generalized Wannier Functions (SNGWFs), defined by

$$|\tilde{\varphi}_m\rangle = |\phi_\alpha\rangle\langle\phi^\alpha|\varphi_m\rangle = |\phi_\alpha\rangle (S^{-1})^{\alpha\beta} \langle\phi_\beta|\varphi_m\rangle. \quad (3)$$

Thus, the final impurity subspace is a proper subspace of the converged Kohn-Sham Hilbert space, a necessary condition for a strictly causal self-energy, but retains the $3d$ symmetry of the numerical atomic orbitals (the generalization to nonorthogonal projector functions in this context is discussed extensively in Ref [26]).

Once the fully-converged DFT energy minimization of was carried out, for each heme strain, the full Green's function was initially computed in the finite-temperature Matsubara representation. Noting that the inverse of a doubly-covariant tensor is a doubly-contravariant tensor, the full Green's function is generally expressed and computed, in terms of the the Kohn-Sham Hamiltonian \mathbf{H} , as

$$G^{\alpha\beta}(i\omega_n) = ((i\omega_n + \mu)S_{\alpha\beta} - H_{\alpha\beta} - \Sigma_{\alpha\beta})^{-1}. \quad (4)$$

Here, μ is the chemical potential, set to the average of the highest occupied and lowest unoccupied Kohn-Sham orbital energies, and Σ is the self-energy tensor generated by the DMFT algorithm, where $\Sigma = \mathbf{0}$ in the first instance so that the initial full Green's function is the Kohn-Sham Green's function \mathbf{G}_0 . Green's function sampling at 400 Matsubara frequencies provided adequate convergence of the properties of interest. We performed this matrix inversion, as well as all matrix multiplications involved in the DMFT algorithm, on graphical computational units (GPUs) using a tailor-made parallel implementation of the LU decomposition using the CUDA programming language. This provided a crucial improvement in the computational feasibility of our calculations. Following inversion to find the the full Green's function, the Kohn-Sham subspace Green's function $\tilde{\mathbf{G}}_0$ is given by its projection onto the impurity subspace, where it

has the matrix representation

$$\begin{aligned} \tilde{\mathbf{G}}_{0mm'}(i\omega_n) &= \langle\tilde{\varphi}_m|\hat{G}(i\omega_n)|\tilde{\varphi}_{m'}\rangle \\ &= W_{m\alpha}G^{\alpha\beta}(i\omega_n)V_{\beta m'}, \end{aligned} \quad (5)$$

where m and m' run over the five iron $3d$ SNGWF projector functions (in real cubic-harmonic notation: $d_{x^2-y^2}$, $d_{3z^2-r^2}$, d_{yz} , d_{xz} , d_{xy}), α and β are the indices for the NGWFs, and the matrices NGWF-projector overlap matrices are defined as $V_{\alpha m}^{(I)} = \langle\phi_\alpha|\varphi_m^{(I)}\rangle$ and $W_{m\alpha}^{(I)} = \langle\varphi_m^{(I)}|\phi_\alpha\rangle$.

In practice, in order to imbue the SNGWF Hubbard projectors with a more plausible physical interpretation, a real-space rotation of the functions was carried out [27] in order to better align their lobes. The subspace projected Green's function is thus transformed to

$$\tilde{\mathbf{G}}^{\text{rot}} = \tilde{\mathbf{U}}^\dagger \tilde{\mathbf{G}} \tilde{\mathbf{U}}, \quad (6)$$

where $\tilde{\mathbf{U}}$ is the 5×5 rotation matrix in cubic harmonic space, corresponding to a rotation in $R^{(3)}$, and $\tilde{\mathbf{G}}^{\text{rot}}$ is the rotated subspace Green's function passed to the DMFT solver. The rotation matrix $\tilde{\mathbf{U}}$ is chosen, pragmatically, such that the \mathbf{e}_x and \mathbf{e}_y axes are those, in an averaged sense, which point towards the four nitrogen atoms surrounding the iron-centered impurity subspace, with \mathbf{e}_z directed out of the porphyrin plane.

Electronic correlation effects beyond the capacity of the approximate exchange-correlation functional, those arising due to interactions between particles within the impurity subspace and finite-temperature effects, are explicitly described in our DMFT calculations by the Slater-Kanamori form of the Anderson impurity Hamiltonian [28, 29], specifically

$$\begin{aligned} \mathcal{H}_U &= U \sum_m n_{m\uparrow}n_{m\downarrow} + (U' - \frac{J}{2}) \sum_{m>m'} n_m n_{m'} \\ &\quad - J \sum_{m>m'} \left(2\mathbf{S}_m \mathbf{S}_{m'} + \left(d_{m\uparrow}^\dagger d_{m\downarrow}^\dagger d_{m'\uparrow} d_{m'\downarrow} \right) \right). \end{aligned} \quad (7)$$

In this, the first term describes the effect of intra-orbital Coulomb repulsion, parametrised by U , and the second term describes the inter-orbital repulsion, proportional to U' , which is renormalized by the Hund's exchange coupling parameter J in order to ensure a fully rotationally invariant Hamiltonian (for further information on this topic, we refer the reader to Ref. [30]). The third term is the Hund's rule exchange coupling, described by a spin exchange coupling of amplitude J . \mathbf{S}_m denotes the spin corresponding to orbital m , so that $S_m = \frac{1}{2} d_{ms}^\dagger \boldsymbol{\sigma}_{ss'} d_{ms'}$, where $\boldsymbol{\sigma}$ is the vector of Pauli matrices indexed by s and s' . We note that the Slater-Kanamori form of the vertex interaction is especially well suited to capture the multiplet properties of the low energy states [30]. The Slater-Koster [31] interaction is another alternative, but is mostly used to describe solids, and is not well suited to the case of a molecule.

In this work, unless where otherwise stated, we used $U = 4$ eV for the screened Coulomb interaction [32] and we explored the dependence of several observables on the Hund's coupling (in the range $J = 0 - 2.5$ eV). Our DMFT calculations were carried out at room temperature, $T = 294$ K, again except where otherwise stated. The dependence of our results with respect to the Coulomb repulsion U and the temperature T is also discussed in the next sections.

METHODOLOGY: DYNAMICAL MEAN-FIELD THEORY TREATMENT

The Hamiltonian (7), in combination with the expressions (4) and (5), defines the many-body impurity problem that we solve using the DMFT algorithm [3], which updates the impurity Green's function $\tilde{\mathbf{G}}$. The DMFT establishes a self-consistent mapping from the correlated atoms of the initial solid or molecule and a smaller local problem, the Anderson Impurity Model (AIM), which is used to obtain the self energy within this projected subspace [3]. The mapping is carried out self-consistently, and the obtained local Green's function of the AIM converges to the Green's function of the larger space projected onto the correlated atom. At the level of the AIM, this model describes an impurity connected to a bath by the so-called hybridization function. The bath of the AIM models the surrounding environment of the correlated atom in the solid or the molecule, and the hybridization function describes how electrons are dynamically transferred from and to the bath to the impurity. Hence, at the AIM level, the uncorrelated part of the Heme molecule is described by the bath, and the hybridization between the d orbitals of the iron atom and the N atoms is described by the hybridization function in the AIM.

We define only a single impurity subspace in calculations on heme, since there is only one transition-metal ion present, and so the impurity self-energy

$$\tilde{\Sigma} = \tilde{\mathbf{G}}_0^{-1} - \tilde{\mathbf{G}}^{-1} \quad (8)$$

resulting from the DMFT algorithm is said to be exactly *local*, in the sense that there are no pairs of impurity sites for which to consider site off-diagonal self-energy matrix elements. In this particular case, there is no feedback from the self energy to the hybridization function, and the DMFT converges after one iteration. It is hence not a mean-field approximation in this particular case, but turns out to be exact. However, the methodology described in this work can be applied to molecules with many correlated ions with no further modifications.

The hybridization matrix Δ within the AIM impurity subspace is given, formally, by

$$\Delta(i\omega_n) = (i\omega_n + \mu) \tilde{\mathbf{O}} - \tilde{\Sigma} - \mathbf{E}^{\text{imp}} - \tilde{\mathbf{G}}^{-1}, \quad (9)$$

where here [33–35], the metric tensor on the SNGWFs is given by

$$\tilde{\mathbf{O}} = (\mathbf{W}\mathbf{S}^{-1}\mathbf{V})^{-1}. \quad (10)$$

This metric is in general non-trivial, i.e., $\tilde{\mathbf{O}} \neq \mathbf{1}$ and so the SNGWFs are nonorthogonal and not identical to their duals, even if their parent atomic orbitals form an orthonormal set, if the trial impurity subspace does not form a proper subspace of the converged Kohn-Sham Hilbert space. However, for this particular case of study, we found however that the deviation of $\tilde{\mathbf{O}}$ from the identity matrix was small (within 0.1%).

The high-frequency part of the hybridization function, $\mathbf{E}^{\text{imp}} = \Delta(i\omega_n \rightarrow \infty)$, defines the impurity energy levels in the zero-hybridization “atomic” limit, so that the hybridization matrix $\Delta(i\omega_n)$ exhibits the correct physical decay proportional to $1/i\omega_n$. We tested that the implied limiting condition $\tilde{\mathbf{O}} = \lim_{\omega \rightarrow \infty} [\tilde{\mathbf{G}}^{-1}(i\omega)''/\omega]$ holds, up to a high precision, ensuring that the self-energy is physically meaningful. It can also be straightforwardly obtained by doing a high frequency expansion of the Green's function that:

$$E^{\text{imp}} = \tilde{\mathbf{O}}\mathbf{W}(\mathbf{S}^{-1}\mathbf{H}\mathbf{S}^{-1})\mathbf{V}\tilde{\mathbf{O}}. \quad (11)$$

The self-energy $\tilde{\Sigma}$ is thus obtained by solving the Anderson impurity model (AIM) defined by the hybridization (9) and the interaction Hamiltonian (7), using a finite-temperature Lanczos DMFT algorithm [36–38]. The Lanczos solver uses a finite discretization of the hybridization (9), suffering finite size effects, yet allows for the orbital off-diagonal elements of the hybridization (9) to be considered on an equal footing to the diagonal elements. Crucially, this mitigates some of the dependence on the spatial form and orientation of the projector functions (SNGWFs) used to define the impurity subspace.

Having solved for impurity self-energy given by the AIM, $\tilde{\Sigma}^{\text{rot}}$, it is rotated back to the original system of coordinates, to give

$$\tilde{\Sigma} = \tilde{\mathbf{U}}\tilde{\Sigma}^{\text{rot}}\tilde{\mathbf{U}}^\dagger. \quad (12)$$

We then “up-fold” it to the Kohn-Sham Hilbert space, using its separable form in terms of NGWFs, that is

$$\Sigma_{\alpha\beta} = V_{\alpha m} \left(\tilde{\Sigma}^{mm'} - V_{\text{dc}}\tilde{\mathbf{O}}^{mm'} \right) W_{m'\beta}. \quad (13)$$

A separable form of the up-folded self-energy enforces its causality, as shown recently in Ref [39], (the local self-energy for the impurity subspace being causal by construction, so that $\tilde{\Sigma}^{mm'}(i\omega_n)'' \leq 0$, for all $i\omega_n, m, m'$). We carefully verified that our computed self-energies were causal, a necessary condition for positive definite spectral functions and the physicality of computed observables

generally. In this work, we used the canonical form of the double-counting potential V_{dc} , given by

$$V_{\text{dc}} = U^{av} \left(n_d - \frac{1}{2} \right) - \frac{J}{2} (n_d - 1), \quad (14)$$

where n_d is the invariant total occupancy of the impurity subspace,

$$n_d = \frac{2}{\pi} \int_0^\mu d\omega \tilde{G}_{mm'}(\omega) \tilde{O}^{m'm}. \quad (15)$$

Here, the parameter U^{av} is the averaged repulsion, related to the intra-orbital and inter-orbital repulsion, and computed using the expression [40]

$$U^{av} = \frac{U + 2(N_{\text{deg}} - 1)U'}{2N_{\text{deg}} - 1}, \quad (16)$$

where $N_{\text{deg}} = 5$ is the number of localised orbitals (SNG-WFs) spanning the impurity subspace. The double-counting correction is intended to subtract the interactions within in the impurity subspace that are already included, to some extent, in the Kohn-Sham Hamiltonian \mathbf{H} . This is carried out in an approximate, averaged fashion, since the exact form of double-counting correction required for a given density, exchange-correlation functional, and set of projecting orbitals, is not known. A good test of the validity of the double-counting correction, verified in our calculations, is the independence of the impurity chemical potential with respect to the Coulomb interaction parameter U . The equations (4), (5), (9), and (13) together form the Green's function self-consistency cycle used in our DFT+DMFT calculations, which is iterated until convergence is obtained. In the calculations presented in this work, for reasons aforementioned, the mapping onto the AIM is effectively exact, and the DFT+DMFT self-consistency cycle converges rapidly, being already close stationary after a single iteration.

METHODOLOGY: IRON DENSITY AND MAGNETIZATION, ENTANGLEMENT AND ENTROPY

Once the AIM problem is solved with the finite temperature Lanczos algorithm, we have access to the ground state and the low energy excited states. The eigenstates of the many-body Hamiltonian are written in the Fock space of the impurity connected to the bath. The basis states of the Fock space span all the possible electronic configurations, hence an eigenstate of the hamiltonian is a superposition of all possible quantum states of the impurity and the bath. It is important to note that other simpler approaches, such as the so-called *Configuration interaction* [41] only consider a very restricted basis set where a few electrons are excited from the impurity to

the bath. In our approach, this is not the case, and all possible configurations are taken into account.

Observables related to the impurity model, such as the impurity density, can be obtained by the finite temperature thermal average. The trace of an operator \hat{A} is defined as:

$$\langle \hat{A} \rangle = \frac{\sum_i e^{-\beta E_i} \langle i | \hat{A} | i \rangle}{Z}, \quad (17)$$

where Z is the partition function, $\beta = 1/T$ is the inverse temperature, and the index i runs over the low energy states. The impurity density operator n_d is simply defined as:

$$\hat{n}_d = \sum_{\sigma} c_{i\sigma}^{\dagger} c_{i\sigma} \quad (18)$$

where $c_{i\sigma}^{\dagger}$ ($c_{i\sigma}$) creates (destroys) an electron in the orbital i of the iron d manifold with spin σ . The thermal average of n_d is given by:

$$\langle n_d \rangle = \frac{\sum_{i,\alpha,\sigma} e^{-\beta E_i} \langle i | c_{\alpha\sigma}^{\dagger} c_{\alpha\sigma} | i \rangle}{Z}, \quad (19)$$

where α denotes the 5 d orbitals, i runs over the eigenstates of the AIM, which is determined self-consistently by the DMFT, E_i is the eigen energy of the quantum eigen state $|i\rangle$. We note that the summation over the eigenstates $|i\rangle$ involves states with different number of electrons, and hence n_d is not an integer number, but can take any rational values. Since upon DMFT convergence the impurity Green's function converges to the Green's function of original problem, the density n_d of the impurity model corresponds to the electronic occupation of the iron atom in heme.

We note that, although the total number of electrons, and global observables more generally, are associated with operators that commute with the Hamiltonian and, hence, are conserved quantities, the density at the iron site is a local observable and can fluctuate strongly.

In particular, we find for $J = 0$ eV that DFT+DMFT yields an impurity occupancy of 6.8 e for deoxyheme, (both for FeP-p and FeP-d), with larger subspace occupancies for ligated hemes ($n_d = 7.0$ e for FeP(CO) and $n_d = 6.9$ e for FeP(O₂)). This is in good agreement with earlier DFT+ $U = 6$ eV calculations [42], which gave $n_d = 6.6$ e for deoxyheme and $n_d = 6.8$ e for carboxyheme. We note that doming of the heme molecule has no effect on the subspace occupancy at small Hund's coupling, although a significant dependence of the occupancy on the doming is activated beyond $J \approx 0.3$ eV.

In our calculations we found that the DMFT solution remains paramagnetic, although it was allowed for the possibility to spontaneously form a magnetic moment (spin symmetry broken state). However, the low energy states are in a quantum superposition of polarized states,

giving a fluctuating magnetic moment at the iron site, which can be quantified as [43]:

$$S = \sqrt{\langle \hat{\mathbf{S}}\hat{\mathbf{S}} \rangle - (\langle \hat{\mathbf{S}} \rangle)^2} = \sqrt{\langle \hat{\mathbf{S}}\hat{\mathbf{S}} \rangle} \quad (20)$$

Where S is the obtained magnetic moment of the iron atom, \mathbf{S} the total spin operator at the iron site. The spin s is obtained as usual by the relation:

$$S = s(s + 1). \quad (21)$$

We note that the eigenstates obtained by the Lanczos are written in the Fock space which contains both the impurity orbitals and the bath orbitals, and although the iron density \hat{n}_d operator is defined in terms of d orbitals, the low energy states are defined in the basis of both the impurity and the bath orbitals. The entanglement between the impurity and the bath can be quantified by the reduced density matrix of the impurity $\hat{\rho}$, defined as:

$$\hat{\rho} = \sum_i e^{-\beta E_i} Tr_B |i\rangle\langle i|, \quad (22)$$

where Tr_B denotes the partial trace over the bath degrees of freedom, and $|i\rangle$ are the low energy states of the problem.

In particular, the eigenvectors \mathbf{v}_k of $\hat{\rho}$ provide a simplified description of the many body states spanned by the impurity: they give a cartoon picture in terms of electronic orbitals for the impurity at low energy. The eigenvalues of $\hat{\rho}$, λ_k are normalized weights ($\sum_k \lambda_k = 1$) which give the probability to measure the corresponding many body state. We note that:

- each \mathbf{v}_k is a superposition of many body states of the Fock space, so it is a quantum superposition of electronic occupations of the impurity orbitals
- there is in general not only one dominant λ_k , but a collection of eigenvalues with similar amplitudes.

The Von Neuman entropy, defined as:

$$\Lambda = -k_B \sum_k \lambda_k \ln(\lambda_k) \quad (23)$$

measures the entanglement between the impurity and the bath. When a number of λ_k with similar amplitudes starts to proliferate, the entropy becomes large. In the particular case when $\lambda_1 = 1$, the impurity is in a pure state and the associated entropy $\Lambda = 0$. In the latter case, the quantum state of the impurity is well defined, and a spin and a charge can be used to label the ground state of impurity problem.

As discussed in the last section, since in the case of DMFT applied to heme there is only one correlated site, the impurity observables, such as the impurity density

n_d or the entropy Λ , readily provide respectively the iron charge density and the entropy associated with the iron atom in the heme molecule. Hence, if the impurity in the AIM is in a pure state ($\Lambda = 0$), one might associate to the heme molecule a charge density and a spin. For the general case $\Lambda > 0$, the iron atom in the heme molecule does not have a fixed spin and valence. This is essentially related to the fact that the iron density and spin are not global observable, and hence they can fluctuate strongly.

We emphasize that the valence fluctuations are not only captured by DMFT, in particular local observables also fluctuate in density functional theory. However the scheme above, only valid for a many body description (Fock space), does not apply at the DFT level and a different definition of the entropy needs to be called for. To characterize the entropy in DFT, the so-called *linear entropy* definition needs to be used [44]. The linear entropy of the reduced density matrix ρ_{red} ,

$$L = Tr(\hat{\rho}_{red}) - Tr(\hat{\rho}_{red}^2) \quad (24)$$

may be used as a measure of entanglement for a pure state. Since the reduced density matrix is normalized ($Tr \hat{\rho}_{red} = 1$), we obtain:

$$L = 1 - Tr(\hat{\rho}_{red}^2) \quad (25)$$

With this definition of the entropy, suitable for DFT calculations, we found that $L = 0.757$ in FeP-p and $L = 0.765$ in FeP-d. The entropy at the DFT level is hence much smaller than the DFT+DMFT entropy, which is in the range $\Lambda = 2.5 - 4.2$. This is explained by the absence of the many-body excitations induced by the correlations (U and J) which contribute significantly to the entropy.

We note that the linear entropy is an approximation of the Von Neumann entropy, which is often used in DFT calculations since it does not require a direct inversion of the full density matrix ρ . Although in principle the DFT entropy obtained for the exact density matrix ρ would capture the effect of quantum entanglement at zero temperature, in practice approximation are made for the exchange energy functional E_{xc} , which in general do not fully capture quantum fluctuations (the extent to which DFT reproduces the entanglement can be studied in simple problems where the exchange functional is known exactly, such as in the Hooke's atom [44]).

A simple many body version can be constructed from the DFT reduced density matrix ρ_{red} in the spirit of the configuration interaction approach, where we have many body states. In the reduced subspace, if we neglect strong off-diagonal components in the DFT reduced density matrix ρ_{red} , the statistical operator is diagonal, and we can associate to each orbital a many body configuration with a statistical weight based on the occupation density of this orbital n and on the averaged double occupancy of this orbital d . In particular, we associate to each orbital

α [45]:

$$\hat{\rho}_\alpha = p_0|0\rangle\langle 0| + \sum_\sigma p_1|\sigma\rangle\langle\sigma| + p_2|2\rangle\langle 2| \quad (26)$$

where $|0\rangle, |\sigma\rangle, |2\rangle$ denotes respectively no electron, an electron with spin σ , and two electrons in the orbital α . A natural estimation of p_0, p_1 and p_2 is:

- $p_0 = 1 - n + d$
- $p_1 = n/2 - d$
- $p_2 = d$

Because of its diagonal form the local von Neumann entropy is given by $\Lambda = -\sum_a p_a \ln p_a$, with $a = 0, \uparrow, \downarrow, 2$ and the total entropy for the five orbitals α can be obtained similarly. To obtain an upper bound on the entropy, we can consider the case without correlations $U = 0$ and assume $d = n^2/4$. We find $\Lambda = 4.72$ for FeP-p and $\Lambda = 4.76$ for FeP-d. These values are of the same order at the maximum of the entropy obtained with DMFT in the regime $J \approx 0.8\text{eV}$.

In particular, in the simple argument above, we assumed that the probabilities associated with every orbital α were independent (no correlations). This simple picture breaks in the presence of a finite U . Indeed, we find that for $J = 0\text{eV}$ and $U = 4\text{eV}$ the entropy is much smaller. A large repulsion quite generally reduces the entropy and orders the charge [45].

In conclusion, to take into account many body effects in the presence of correlations in the iron atom (U and J), a consistent method is required. DMFT provides a framework to carry out these calculations without any add-hoc assumptions.

METHODOLOGY: SPECTRAL FUNCTIONS RESOLVED IN REAL-SPACE AND ENERGY, THE OPTICAL CONDUCTIVITY AND THE TOTAL ENERGY

The Lanczos DMFT solver used in our study [46] readily provides information on the real frequency axis. For example, the NGWF-resolved spectral density $\rho_{\alpha\beta}(\omega)$ is defined, via the retarded Green's function obtained at DMFT self-consistency, \mathbf{G} , by

$$\rho^{\alpha\beta}(\omega) = \frac{G^{\alpha\beta}(\omega) - G^{\dagger\alpha\beta}(\omega)}{2i\pi}. \quad (27)$$

We note that the Green's function has poles on the real axis, such that it is in principle not possible to define $G(\omega)$. Hence, the Green's function is defined with a small but finite broadening factor $i\eta$, and $G(\omega + i\eta)$ is used in the formula above. The small shift η plays the role of a broadening factors, similarly to the broadening used in

DFT to compute the density of states at zero temperature.

The DFT+DMFT density of states is then given by the imaginary part of the many-body density matrix, so that

$$\rho(\omega) = \Im [\rho^{\alpha\beta}(\omega)] S_{\beta\alpha}. \quad (28)$$

The real-space representation of the *Fermi density*, the spectral density at the Fermi level is given by

$$n_F(\mathbf{r}) = \phi_\alpha(\mathbf{r}) \Im [\rho^{\alpha\beta}(\omega \rightarrow \mu)] \phi_\beta(\mathbf{r}). \quad (29)$$

The theoretical optical absorption was obtained in DFT+DMFT within the linear-response regime (Kubo formalism), including the effect of non-local pseudopotentials on the velocity operator matrix elements [47], in the *no-vertex-corrections* approximation [48], where it is given by:

$$\sigma(\omega) = \frac{2\pi e^2 \hbar}{\Omega} \int d\omega' \frac{f(\omega' - \omega) - f(\omega')}{\omega} \times (\rho^{\alpha\beta}(\omega' - \omega) \mathbf{v}_{\beta\gamma} \rho^{\gamma\delta}(\omega') \mathbf{v}_{\delta\alpha}), \quad (30)$$

and the factor of two accounts for spin-degeneracy, Ω is the simulation-cell volume, e is the electron charge, \hbar is the reduced Planck constant, $f(\omega)$ is the Fermi-Dirac distribution, and the many-body density matrix $\rho^{\alpha\beta}$ is that defined by equation (27). We note that the optical conductivity will be smoothed out by the broadening parameter $i\eta$ used to obtain the Green's function on the real axis. In practice, $i\eta$ is chosen to be small enough such that the important features in the optics can be identified.

The matrix elements of the velocity operator along one of the direction $\mathbf{e}_x, \mathbf{e}_y, \mathbf{e}_z$, denoted as $\mathbf{v}_{\alpha\beta}^j$ ($j = (x, y, z)$) are given by

$$\mathbf{v}_{\alpha\beta}^j = -\frac{i\hbar}{m_e} \langle \phi_\alpha | \nabla_j | \phi_\beta \rangle + \frac{i}{\hbar} \langle \phi_\alpha | [\hat{V}_{nl}, \mathbf{r}] | \phi_\beta \rangle. \quad (31)$$

This expression is general to the nonorthogonal NGWF representation [49], used in this work, where the contribution to the non-interacting Hamiltonian due to the non-local part of the norm-conserving pseudopotentials, [50, 51] represented by \hat{V}_{nl} , is included. It is worth noting that we do not invoke the Peierls substitution [48].

Since optical experiments on heme are typically carried out in liquid or gas phases, therefore the isotropic part of the optical conductivity tensor:

$$\sigma(\omega) = \sum_i \sigma_{ii}(\omega) / 3, \quad (32)$$

is of primary interest. Finally, we note that optical transitions between hybridised d orbitals (d-d transition type) are forbidden by optical selection rules if the hybridization of the d and p-orbitals happens in a perfect octahedral symmetry, such as in FeP-p.

Once the self energy matrix is obtained, it can be used to correct the DFT total energy with the DMFT correction. The total energy is estimated by the functional [52, 53]:

$$E = E_{LDA}(\rho(\mathbf{r})) - \sum_{\mathbf{k}\nu}' \epsilon_{\mathbf{k}\nu} + \text{Tr} \left[\hat{H}_{LDA} \hat{G} \right] + \langle \hat{H}_U \rangle - E_{DC} \quad (33)$$

where \hat{H}_U indicates the many body interaction vertex of the DMFT, and the primed sum is over the occupied states. The symbol "Tr" indicates the one-electron trace for a generic representation and the sum over the Matsubara frequencies $i\omega_n$ for finite-temperature many-body formalism.

We notice that the total energy within the LDA+DMFT scheme is not simply the expectation value of this Hamiltonian but it consists of several terms, in analogy to the expressions of the usual DFT. The first term E_{LDA} contains four different contributions, namely, the ones due to the external potential, the Hartree potential, the exchange-correlation potential, and the sum of the Kohn-Sham eigenvalues. However in the spectral density-functional theory, the Kohn-Sham eigenvalues should be reoccupied with respect to the description given by the total Greens function. Then we should remove the bare Kohn-Sham eigenvalues sum (second term) and substitute it with $\text{Tr} \left[\hat{H}_{LDA} \hat{G} \right]$ (third term).

The interaction term \hat{H}_U can be obtained with the the Galitskii-Migdal formula [54]:

$$\langle \hat{H}_U \rangle = \frac{1}{2} \text{Tr} \left[\hat{\Sigma} \hat{G} \right] \quad (34)$$

Where $\hat{\Sigma}$ (\hat{G}) is the self-energy (Green's function) matrix in the NGWFs representation. We note that both the self energy and the Green's function are slowly decaying function, hence the trace over matsubara frequencies has to be done with care. In this work, we followed the steps of Refs. [52, 53].

Finally, the double-counting correction E_{DC} must be introduced, since the contribution of interactions between the correlated orbitals to the total energy is already partially included in the exchange-correlation potential derived from the DFT. The most commonly used form of the double-counting term is [40]:

$$E_{DC} = \frac{U_{av}}{2} N_d (N_d - 1) - \frac{J}{2} \sum_{\sigma} N_{d\sigma} (N_{d\sigma} - 1) \quad (35)$$

where U_{av} is the averaged Coulomb repulsion defined in equation (16).

VALIDATION OF THE METHODOLOGY

In order to validate our approach, we have studied the dependence of our results with the other parameters of

the theory, e.g. the temperature T and the Coulomb repulsion U .

We show in Fig. 1.a the iron occupation n_d as a function of J for different values of $U = 3.5\text{eV}$, $U = 4\text{eV}$, $U = 4.5\text{eV}$, and $U = 5\text{eV}$ for FeP-d. We find that the results are qualitatively similar, for a 1.5eV variation of U (3.5 – 5eV), although the critical value J associated with the sharp drop of the iron density is slightly shifted from $J = 0.8\text{eV}$ to $J = 1\text{eV}$. We note however that for $J = 0\text{eV}$, the density is only very marginally affected as a function of U . The latter suggest that strong modifications of the physical properties are induced principally by the Hund's coupling. In our work, we chose $U = 4\text{eV}$, in agreement with earlier DFT studies [32], and we show that although variations in U might give some quantitative modifications at $J=0$, there is a dramatic change in the occupation density at finite J , neglected so far in the DFT studies of heme. We also note that it is physically better to take into account the Hund's coupling when dealing with metallic atoms such as iron, known to have a large Hund's coupling.

We also studied how our results depend on the temperature T (see Fig. 1.b). We compared the data obtained at $T = 100\text{K}$ and $T = 293\text{K}$. Despite some minor quantitative differences, the sharp transition in the iron density is obtained for the same critical Hund's coupling J , showing that our predictions are valid for a broad range of physically relevant temperatures. This confirms also that quantum fluctuations are mostly dominating in this regime of temperature, although we cannot exclude that for $T < 100\text{K}$ we might observe some larger changes.

In conclusions, we believe that our predictions are not dependent on the details of our model, and we show that the parameter which has a dramatic impact on the physics in the Hund's coupling.

To support further the justification that the Hund's coupling is important for heme, we now turn to the discussion of the optics for FeP-d (Fig. 2.a), FeP(CO) (Fig. 2.b) and FeP(O₂) (Fig. 2.c) as a function of J . For unligated heme (Fig. 2.a), we do not find any qualitative difference in the optical spectra as J is increased from 0eV to 1.2eV. However, for both FeP(CO) and FeP(O₂), we find that increasing J gives a double peaked structure at $\omega \approx 2\text{eV}$, which is also observed in experiments (see inset of the Fig. 3 of the paper). This double peaked structure, absent for $J = 0\text{eV}$, suggests also that J is important to describe the heme molecule. We note that the best fit to the experiments is obtained for $J = 0.9\text{eV}$, and hence we can furthermore support that the Hund's coupling is consequent in heme based on phenomenological grounds.

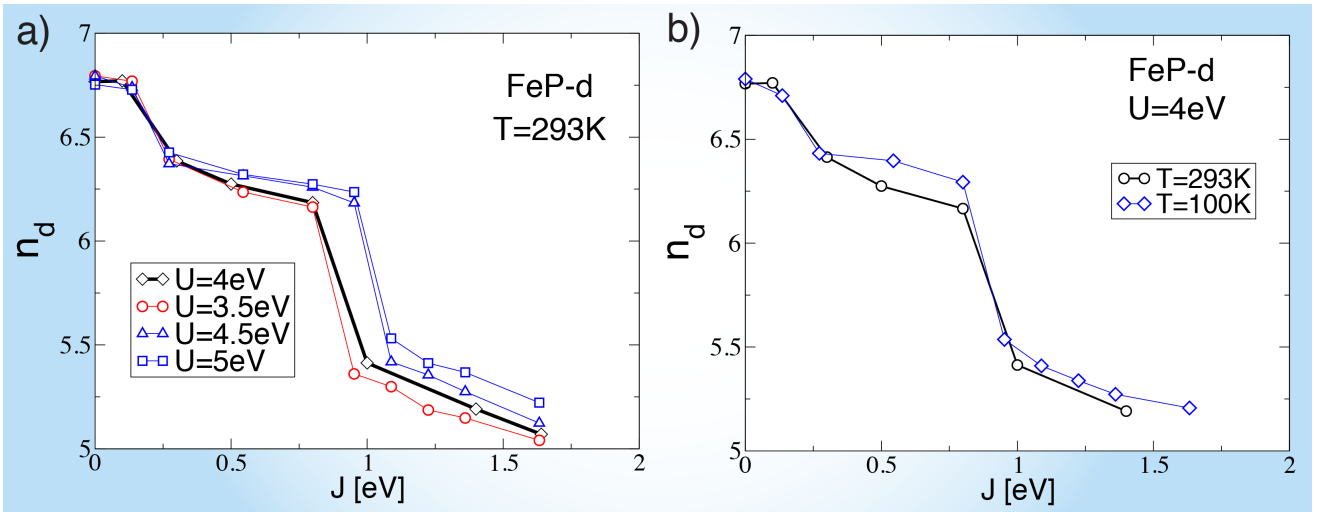


FIG. 1: (Colors online) a) Iron occupation n_d as a function of the Hund's coupling J for different Coulomb repulsion U for FeP-d. The data discussed in the paper are reproduced here for comparison ($U = 4\text{eV}$, bold line). The sharp transition in the iron density is present for all repulsions. b) Iron occupation n_d for two different temperatures $T = 100\text{K}$ (diamonds) and $T = 293\text{K}$ (circles).

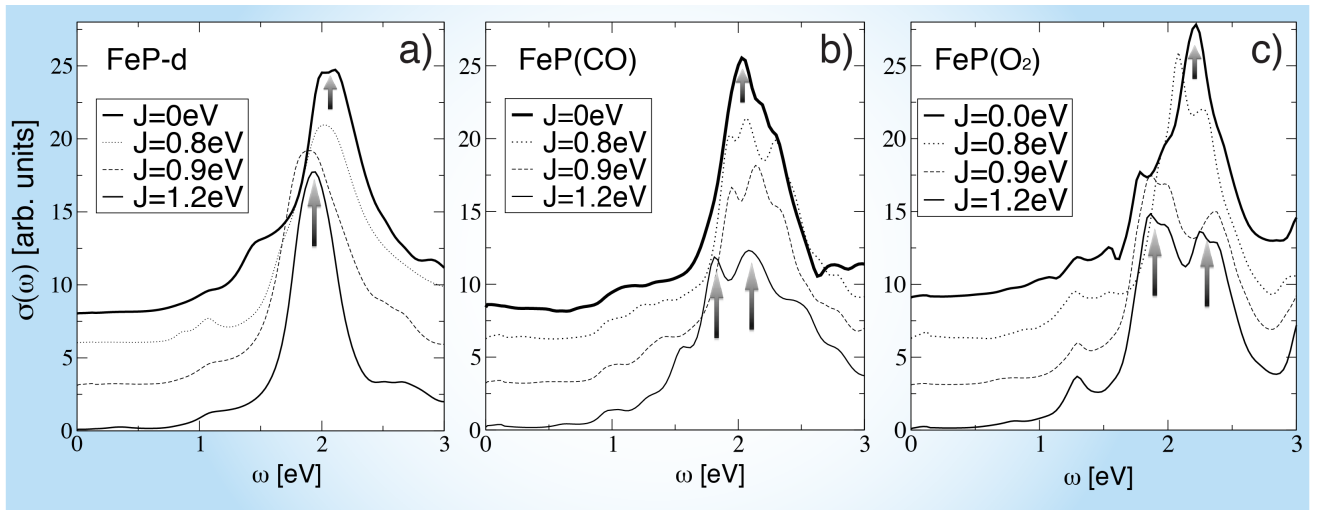


FIG. 2: Optical spectra for a) FeP-d, b) FeP(CO) and c) FeP(O₂) for different values of J (from top to bottom): $J = 0\text{eV}$ (bold line), $J = 0.8\text{eV}$ (dotted line), $J = 0.9\text{eV}$ (dashed line), $J = 1.2\text{eV}$ (full line). The arrows highlight the presence of a single peak structure for $J = 0\text{eV}$, which splits in a double peaked structure as J increases. For clarity, the curves were shifted on the vertical axis.

EFFECT OF THE HUND'S COUPLING ON THE ORBITAL POLARISATION AND BINDING TO LIGANDS

As shown in the Fig. 3a of the paper, the effect of the Hund's coupling is to reduce the difference in the FeP binding energies to CO and O₂ ($\Delta\Delta E$). In this section we give more details regarding the mechanism underlying the reduction of $\Delta\Delta E$ induced by J .

In Fig. 3 we show the energy variation for FeP(CO)

and FeP(O₂) as the Hund's coupling J increases. We find that while the energy of FeP(CO) is only weakly affected by J , there is a sharp drop of the energy of FeP(O₂) at $J \approx 0.8\text{eV}$.

The latter can be understood in terms of orbital polarisations. In particular, we compare in Table I the electron occupation of the iron d orbitals for $J = 0$ and $J = 0.8\text{eV}$. We note that the orbital occupations are not integer numbers. Indeed, in the presence of hybridisation (see Fig. 4.a,b), the atomic iron densities (local observables)

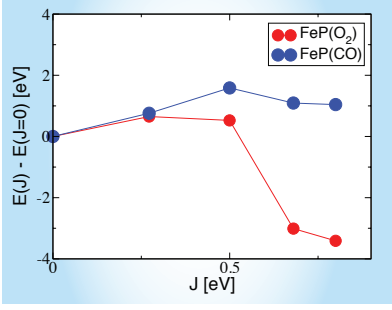


FIG. 3: **Energy:** variation of the total energy $\Delta E = E(J) - E(J = 0)$ of FeP(O₂) (red circles) and FeP(CO) (blue circles) as a function of the Hund's coupling. While there is a drop in the energy for FeP(O₂) at $J \approx 0.8$, the energy of FeP(CO) is only weakly affected by the Hund's coupling.

	J	$d_{x^2-y^2}$	$d_{3z^2-r^2}$	d_{xz}	d_{xy}	d_{yz}
FeP	0	0.85	1.86	1.24	1.98	0.82
FeP	0.8	1.10	1.75	1.08	1.14	1.08
FeP(CO)	0	1.06	0.86	1.99	1.06	1.99
FeP(CO)	0.8	1.14	1.33	1.16	1.05	1.85
FeP(O ₂)	0	0.72	1.82	1.25	1.87	1.28
FeP(O ₂)	0.8	1.03	1.07	1.18	1.97	1.09

TABLE I: Average occupations n_d^α of the iron d orbitals for FeP, FeP(CO) and FeP(O₂), for $J=0$ and $J=0.8$.

are not conserved quantum numbers, and can take fractional values, which is a signature of valence fluctuations.

However, due to the form of the hybridization of the iron atom in FeP, the orbitals ($d_{3z^2-r^2}$, d_{xy}) are almost filled and hence do not fluctuate (Table I) in the absence of the Hund's coupling. We also find that for FeP(CO) and FeP(O₂), the orbital which are almost full are respectively the (d_{xz} , d_{yz}) and the ($d_{3z^2-r^2}$, d_{xy}) orbitals.

The main effect of the Hund's coupling J is to increase the magnetic moment of the iron atom, which in turn yields a concomitant reduction of the iron density n_d . For FeP, there is a reduction of the iron density of 0.52 e (see Table III), induced by the build up of the self energy at the iron site due to the Hund's coupling and the Coulomb repulsion, and a reduction of 0.25 e of the neighbour N atoms. The charge is transferred to the two hydroxyl chains which are electronegative (each hydroxyl chain contains two O atoms).

We find that in FeP(CO), the orbital mostly affected by an increase of J is the d_{xz} : the occupation of the latter is reduced from 2 e ($J = 0$) down to 1.16 e ($J = 0.8$ eV). For FeP(O₂), the orbital which is strongly affected by J is the $d_{3z^2-r^2}$ orbital: the occupation of the latter is reduced from 1.8 e down to 1.07 e. Moreover, we find that the reduction of the occupation of d_{xz} in FeP(CO) and the reduction of the occupation of $d_{3z^2-r^2}$ in FeP(O₂)

	J	$d_{x^2-y^2}$	$d_{3z^2-r^2}$	d_{xz}	d_{xy}	d_{yz}
FeP	0	0.30	0.15	0.28	0.05	0.28
FeP	0.8	0.31	0.20	0.39	0.38*	0.39
FeP(CO)	0	0.37	0.37	0.03	0.48	0.03
FeP(CO)	0.8	0.37	0.40	0.46*	0.48	0.19
FeP(O ₂)	0	0.35	0.20	0.34	0.17	0.34
FeP(O ₂)	0.8	0.37	0.43*	0.45	0.08	0.46

TABLE II: Internal magnetic moment of the iron d orbitals for FeP, FeP(CO) and FeP(O₂), for $J=0$ and $J=0.8$. The internal orbital magnetic moment is obtained by $S_\alpha = \sqrt{\langle \mathbf{S}_\alpha \mathbf{S}_\alpha \rangle}$, where α is an index for the d orbital and \mathbf{S}_α is the spin operator of the orbital α . The star highlights the orbital with the largest moment increase.

atom	$\Delta n(r)$
Iron d orbitals	-0.52
Nitrogen ring	-0.25
hydroxyl groups	+0.77

TABLE III: Variation of the charge $\Delta n(r) = n(r, J = 0.8) - n(r, J = 0)$ in FeP induced by the Hund's coupling.

are consistent with a build up of the magnetic moment in the latter orbitals (see Table II). We note that both the Coulomb repulsion U and the Hund's coupling J have an importance here, and promote different many body configurations. The Coulomb repulsion U tend to suppress doubly occupied many body configurations, whereas the Hund's coupling tends to generate many body configurations with aligned spins. In particular, a physical constraint on the Hund's coupling J is $J < U$ (see Ref. [30]).

The reduction of the charge of the d_{xz} orbital in FeP(CO) and of the $d_{3z^2-r^2}$ orbital in FeP(O₂) is expected to reduce the Coulomb energy, which penalises doubly occupied orbitals. Moreover, the charge reduction is also expected to yield an optimisation of the kinetic energy, since transfer of electrons to a filled orbital are impossible. The latter is however not effective in FeP(CO), since the d_{xz} orbital does not hybridise strongly (see Fig. 4.a) and hence no drastic change is expected in the kinetic energy, but the latter is expected to be important for FeP(O₂) since the $d_{3z^2-r^2}$ orbital hybridise significantly (see Fig. 4.b). This accounts for the further energy reduction in FeP(O₂) at $J \approx 0.8$ eV, not present in FeP(CO), as observed in Fig. 3.

QUANTUM DYNAMICS: TRANSIENT MAGNETIC RESPONSE SIMULATIONS

We analyzed the quantum dynamics of heme by means of out-of-equilibrium calculations performed using a recently-developed implementation of the Keldysh formalism adapted for Lanczos DMFT solvers [55]. Our

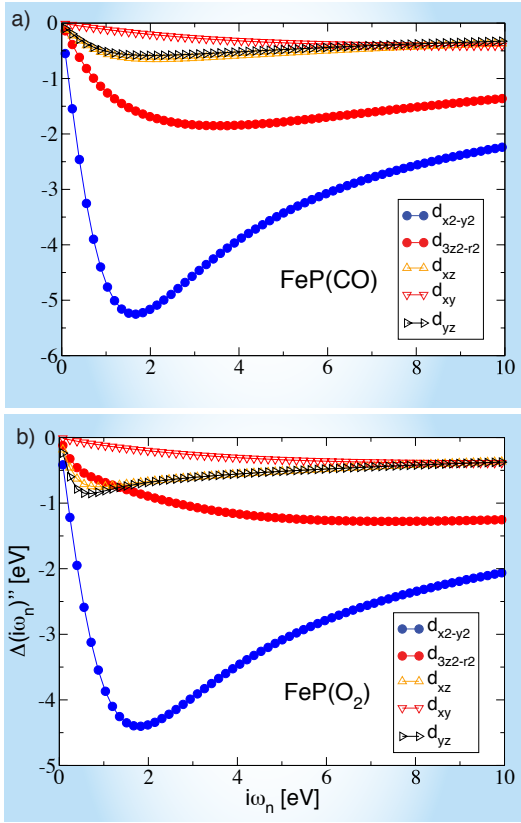


FIG. 4: **Iron dynamical hybridization:** Imaginary part of the hybridization Δ'' as a function of the matsubara frequencies $i\omega_n$ of the iron d orbitals for a) FeP(CO) and b) FeP(O₂). The e_g orbitals have the largest hybridization. Note that the hybridization is independent of the many body parameters U and J .

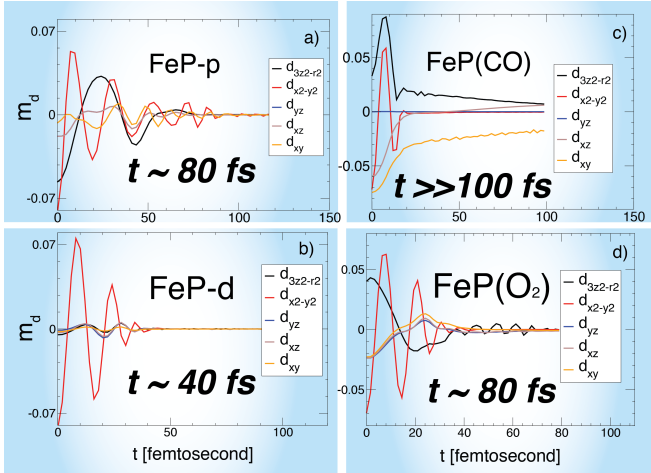


FIG. 5: **Transient magnetic response:** Time dependence of the subspace magnetization $m_d = (n_d^\uparrow - n_d^\downarrow)\hbar/2$, after an initial quench in a magnetic dipole field, for heme species a) FeP-p, b) FeP-d, c) FeP(CO) and d) FeP(O₂).

calculations allow us to directly tackle the issue of dynamical relaxation after a quantum quench; the results are shown in Fig. 5. Specifically, we applied a quench in molecular spin polarization at $t = 0$, by perturbing the ground state with a magnetic dipole impulse applied to the iron $3d$ impurity subspace and thereafter studying the transient behavior of the spin polarization. The heme molecule plays the role of a dissipation bath, such that after a long enough time the system relaxes to the equilibrium. The relaxation times for unligated deoxyheme, at $J = 0.8$ eV, were found to be approximately $t = 80$ fs (Fig. 5.a) and $t = 40$ fs (Fig. 5.b) for FeP-p (unligated, planar) and FeP-d (unligated, domed), respectively. We find that in the FeP-d system, only the $d_{x^2-y^2}$ orbital is strongly spin polarized by the quench, whereas, in FeP-p, the $d_{3z^2-r^2}$ orbital is also partially occupied in the ground-state and hence also participates in the magnetic response, yielding transient oscillations that are longer-lived overall. Our result suggests that the dome-shaped configuration protects heme from external perturbations to some extent, reducing the hybridization between the $d_{x^2-y^2}$ and $d_{3z^2-r^2}$ orbitals by further lifting their degeneracy. For FeP(CO) (Fig. 5.c), we observe a very long relaxation time (beyond our numerical reach); magnetically perturbed FeP(CO) becomes trapped in a metastable state with a slowly-decaying internal magnetization. Finally, for FeP(O₂), we find an intermediate relaxation time of $t = 80$ fs (Fig. 5.d), and transient response rather different to that of FeP(CO), a difference which appears to be primarily due to a magnetic equivalence among the t_{2g} orbitals of FeP(O₂) which is absent in FeP(CO). These results highlight the surprisingly long time-scale and system dependence associated with quantum spin relaxation. Photo-excitation of carboxyheme, FeP(CO), has previously been discussed in the context of both femtosecond spectroscopy [56] and time-resolved resonance Raman spectra [57], where the presence of excited states with a lifetime of 300 fs was attributed to iron-to-porphyrin charge-transfer excitations. We suggest, based on the results of our out-of-equilibrium simulations (Fig. 5), that circularly-polarized two-photon spectroscopy may be used as a sensitive probe for the geometric configuration and ligation state of heme.

- [1] C. Weber, D. D. O'Regan, N. D. M. Hine, M. C. Payne, G. Kotliar, and P. B. Littlewood, *Phys. Rev. Lett.* **108**, 256402 (2012).
- [2] D. D. O'Regan, N. D. M. Hine, M. C. Payne, and A. A. Mostofi, *Phys. Rev. B* **85**, 085107 (2012).
- [3] A. Georges, G. Kotliar, W. Krauth, and M. J. Rozenberg, *Rev. Mod. Phys.* **68**, 13 (1996).
- [4] T. A. Maier, T. Pruschke, and M. Jarrell, *Phys. Rev. B* **66**, 075102 (2002).
- [5] A. Kutepov, K. Haule, S. Y. Savrasov, and G. Kotliar,

- Phys. Rev. B* **82**, 045105 (2010).
- [6] J. M. Tomczak, K. Haule, and G. Kotliar, *Proceedings of the National Academy of Sciences* **109**, 3243 (2012).
- [7] L. de' Medici, J. Mravlje, and A. Georges, *Phys. Rev. Lett.* **107**, 256401 (2011).
- [8] P. Hohenberg and W. Kohn, *Phys. Rev.* **136**, B864 (1964).
- [9] W. Kohn and L. J. Sham, *ibid.* **140**, A1133 (1965).
- [10] N. D. M. Hine, P. D. Haynes, A. A. Mostofi, C.-K. Skylaris, and M. C. Payne, *Computer Physics Communications* **180**, 1041 (2009).
- [11] D. D. O'Regan, N. D. M. Hine, M. C. Payne, and A. A. Mostofi, *Phys. Rev. B* **85**, 085107 (2012).
- [12] N. D. M. Hine, P. D. Haynes, A. A. Mostofi, and M. C. Payne, *The Journal of Chemical Physics* **133**, 114111 (2010).
- [13] C.-K. Skylaris, A. A. Mostofi, P. D. Haynes, O. Diéguez, and M. C. Payne, *Phys. Rev. B* **66**, 035119 (2002).
- [14] A. Mostofi, P. Haynes, C. Skylaris, and M. Payne, *Journal of Chemical Physics* **119**, 8842 (2003).
- [15] R. McWeeny, *Rev. Mod. Phys.* **32**, 335 (1960).
- [16] E. Hernández and M. J. Gillan, *Phys. Rev. B* **51**, 10157 (1995).
- [17] C. Skylaris, P. Haynes, A. Mostofi, and M. Payne, *Journal of Chemical Physics* **122** (2005).
- [18] J. P. Perdew, K. Burke, and M. Ernzerhof, *Phys. Rev. Lett.* **77**, 3865 (1996).
- [19] A. M. Rappe and E. J. Walter, *Opium package*, <http://opium.sourceforge.net>.
- [20] G. Fermi, M. F. Perutz, B. Shaanan, and R. Fourme, *J Mol Biol* **175**, 159 (1984).
- [21] Jmol: an open-source Java viewer for chemical structures in 3D. <http://www.jmol.org/>.
- [22] Y. Naoi, K. T. Chong, K. Yoshimatsu, G. Miyazaki, J. R. Tame, S. Y. Park, S. Adachi, and H. Morimoto, *J Mol Biol* **307**, 259 (2001).
- [23] B. Shaanan, *J Mol Biol* **171**, 31 (1983).
- [24] L. G. G. V. Dias da Silva, M. L. Tiago, S. E. Ulloa, F. A. Reboredo, and E. Dagotto, *Phys. Rev. B* **80**, 155443 (2009).
- [25] M. Aichhorn, M. Daghofer, H. G. Evertz, and W. von der Linden, *Phys. Rev. B* **67**, 161103 (2003).
- [26] D. D. O'Regan, M. C. Payne, and A. A. Mostofi, *Phys. Rev. B* **83**, 245124 (2011).
- [27] J. Ivanić and K. Ruedenberg, *The Journal of Physical Chemistry* **100**, 6342 (1996).
- [28] J. C. Slater, *Phys. Rev.* **49**, 537 (1936).
- [29] J. Kanamori, *Journal of Physics and Chemistry of Solids* **10**, 87 (1959).
- [30] M. Imada, A. Fujimori, and Y. Tokura, *Rev. Mod. Phys.* **70**, 1039 (1998).
- [31] J. C. Slater and G. F. Koster, *Phys. Rev.* **94**, 1498 (1954).
- [32] D. A. Scherlis, M. Cococcion, P. Sit, and N. Marzari, *J. Phys. Chem. B* **111**, 7384 (2007).
- [33] D. Zgid and G. K.-L. Chan, *Journal of Chemical Physics* **134**, 094115 (2011).
- [34] V. S. Oudovenko, G. Pálsson, K. Haule, G. Kotliar, and S. Y. Savrasov, *Phys. Rev. B* **73**, 035120 (2006).
- [35] G. Kotliar, S. Y. Savrasov, G. Pálsson, and G. Biroli, *Phys. Rev. Lett.* **87**, 186401 (2001).
- [36] M. Capone, L. de' Medici, and A. Georges, *Phys. Rev. B* **76**, 245116 (2007).
- [37] A. Liebsch and N.-H. Tong, *Phys. Rev. B* **80**, 165126 (2009).
- [38] C. Weber, C. Yee, K. Haule, and G. Kotliar, *arXiv/1108.3028*.
- [39] K. Haule, C.-H. Yee, and K. Kim, *Phys. Rev. B* **81**, 195107 (2010).
- [40] T. Pruschke and M. Zöflf, in *Advances in Solid State Physics* **40**, Vol. 40, edited by B. Kramer (Springer Berlin / Heidelberg, 2000) pp. 251–265.
- [41] C. D. Sherrill and H. F. S. III (Academic Press, 1999) pp. 143 – 269.
- [42] D. D. O'Regan, *Optimised Projections for the Ab Initio Simulation of Large and Strongly Correlated Systems*, 1st ed., Springer Theses, Vol. XVI (Springer, Berlin, Heidelberg, 2012) p. 225.
- [43] Y. I. Prokopjev and B. I. Reser, *J. Phys.: Condens. Matter* **3**, 6055 (1991).
- [44] J. P. Coe, A. Sudbery, and I. D'Amico, *Phys. Rev. B* **77**, 205122 (2008).
- [45] K. Byczuk, J. Kuneš, W. Hofstetter, and D. Vollhardt, *Phys. Rev. Lett.* **108**, 087004 (2012).
- [46] C. Weber, A. Amaricci, M. Capone, and P. B. Littlewood, *Phys. Rev. B* **86**, 115136 (2012).
- [47] A. J. Read and R. J. Needs, *Phys. Rev. B* **44**, 13071 (1991).
- [48] A. J. Millis, *Strong Interactions in Low Dimensions, Physics and Chemistry of Materials with Low-Dimensional Structures*. **25**, 195 (2004).
- [49] V. Halpern and A. Bergmann, *Journal of Physics C: Solid State Physics* **5**, 1953 (1972).
- [50] L. E. Ratcliff, N. D. M. Hine, and P. D. Haynes, *Phys. Rev. B* **84**, 165131 (2011).
- [51] A. J. Read and R. J. Needs, *Phys. Rev. B* **44**, 13071 (1991).
- [52] I. Di Marco, J. Minár, S. Chadov, M. I. Katsnelson, H. Ebert, and A. I. Lichtenstein, *Phys. Rev. B* **79**, 115111 (2009).
- [53] L. V. Pourovskii, B. Amadon, S. Biermann, and A. Georges, *Phys. Rev. B* **76**, 235101 (2007).
- [54] V. M. Galitskii and A. B. Migdal, *Sov. Phys. JETP* **139**, 96 (1958).
- [55] M. Balzer, N. Gdaniec, and M. Potthoff, *J. Phys.: Condens. Matter* **24**, 035603 (2012).
- [56] P. Anfinrud, C. Han, and R. Hochstrasser, *Proc. Nadl. Acad. Sci. USA* **86**, 8387 (1989).
- [57] S. Franzen, L. Kiger, C. Poyart, and J.-L. Martin, *Biophysical Journal* **80**, 2372 (2001).
- [58] Repeated index pairs are implicitly summed over, as per the Einstein summation convention; enclosure by parenthesis suspends the summation.